

Spiral states, first-order transitions and specific heat multipeak phenomenon in J_1 - J_2 - J_3 Ising model: A Wang-Landau algorithm study

Habib Ullah,^{1,*} Kun Li,^{1,*} Haoyu Lu,¹ Youjin Deng,^{2,3,†} and Wanzhou Zhang^{1,‡}

¹College of Physics, Taiyuan University of Technology, Shanxi 030024, China

²Hefei National Laboratory for Physical Sciences at the Microscale and Department of Modern Physics,

University of Science and Technology of China, Hefei 230026, China

³Hefei National Laboratory, University of Science and Technology of China, Hefei 230088, China

(Dated: December 30, 2025)

The classical J_1 - J_2 - J_3 Ising model on the honeycomb lattice is important for understanding frustrated magnetic phenomena in materials such as FePS_3 and $\text{Ba}_2\text{CoTeO}_6$, where diverse phases (e.g., striped, zigzag, armchair) and magnetization plateaus have been experimentally observed. To explain the experimental results, previous mean-field studies have explored its thermal phase transitions, identifying armchair phases and striped phases, but their limitations call for more reliable numerical investigations. In this work, we systematically revisit the classical J_1 - J_2 - J_3 Ising model using the Wang-Landau algorithm. We find that the armchair (AC) phase, previously reported in mean-field and experimental studies, actually coexists with the spiral (SP) phase, with their combined degeneracy reaching 20-fold (4-fold for the AC states and 16-fold for the spiral states). The phase transitions and critical exponents are studied at different interaction values. We observe first-order phase transitions, continuous phase transitions, and even the multipeak phenomenon in frustrated systems. These results clarify the nature of phases and phase transitions in frustrated Ising systems and their exponents, and additionally provide inspiration for experimental efforts to search for the spiral state and specific-heat multipeak phenomenon.

I. INTRODUCTION

Frustrated spin models have long been a central topic in condensed matter physics [1]. A prototypical example is the J_1 - J_2 - J_3 spin model, which incorporates nearest-neighbor (J_1), next-nearest-neighbor (J_2), and third-nearest-neighbor (J_3) interactions. On honeycomb lattices, the quantum variant of this model—such as the Heisenberg model, exhibits a rich array of phenomena, including spiral spin states [2–5]. In particular, even when $J_3 = 0$, the system sustains a spin liquid phase [6, 7], while its spin-1 counterpart displays distinct magnetic behavior [8]. The study of these quantum systems has been significantly advanced by numerical techniques, particularly the density matrix renormalization group [9] and tensor network approaches [5, 10].

Without quantum fluctuations, the classical J_1 - J_2 - J_3 Ising model was used to describe magnetic materials, such as FePS_3 , a prime example of a two-dimensional Ising-like antiferromagnet on a honeycomb lattice formed by Fe^{2+} ions [11]. Other experiments related to the honeycomb lattice, such as $\text{Ba}_2\text{CoTeO}_6$ [12], where Co^{2+} ions form the honeycomb lattice. A variety of spin-density wave phases have been observed in these experimental systems, such as the striped phase, the zigzag phase, the armchair (AC) phase, and various magnetization plateaus upon the application of a magnetic field

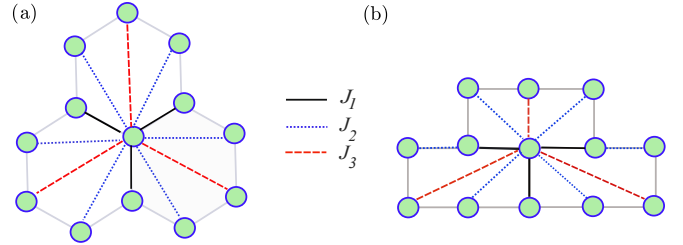


Figure 1. The lattice structure of a honeycomb lattice is shown in (a) for the hexagonal representation and in (b) for the square-like arrangement, with J_1 , J_2 , and J_3 representing the nearest-neighbor, second-nearest neighbor, and third-nearest neighbor interactions, respectively.

[11].

To explore these phenomena, pioneering theoretical studies using the mean-field (MF) approach by Refs. [13, 14] have examined the thermal phase transitions of the J_1 - J_2 - J_3 Ising model in the honeycomb lattices. In the range $J_3/J_1 < 1/2$, the armchair phase is found. In the range $J_3/J_1 > 1/2$, interesting criticality and tricriticality are found. Due to the limitations of mean-field methods, the authors [13] also call on researchers to use more powerful Wang-Landau (WL) algorithms or parallel tempering (PT) algorithms [15–19] to further explore the nature of phase transitions in this system [20]. In fact, exploring such frustrated systems on various lattices poses enormous challenges due to their strong groundstate degeneracy [21].

In this paper, we systematically revisit the J_1 - J_2 - J_3 model on the honeycomb lattice using the WL al-

* These two authors contributed equally to this paper.

† yjdeng@ustc.edu.cn

‡ zhangwanzhou@tyut.edu.cn

gorithm [15–19]. In the strong frustration region, PT method is also used as an auxiliary approach.

The main findings are as follows. The AC phase revealed in MF studies [13, 14] and experiments [11] coexists with the spiral (SP) phase in the intermediate parameter regime: the AC state is 4-fold degenerate, while the spiral state is 16-fold degenerate, leading to a total 20-fold degeneracy. Another key result is that, guided by the MF phase diagram, we accurately and reliably determine the ST-PM and AC+SP-PM phase transition boundaries at $J_3/J_1 = 1.2, 0.6, 0.2$, identify their transition types, and derive the corresponding critical exponents via the Wang-Landau algorithm. Additionally, in the strong frustration regime $J_2/J_1 = -1.5$ and $J_3/J_1 = 0.2$ the specific heat exhibits a multi-peak behavior [22].

The outline of our paper is as follows. Sec. II presents the $J_1-J_2-J_3$ model, the WL method, and the measured quantities. The results on the phase diagram and details are shown in Sec. III. The conclusion and discussion are given in Sec. IV

II. THE MODEL, METHOD AND QUANTITIES

A. $J_1-J_2-J_3$ Ising model

The Hamiltonian is given below.

$$H = - \sum_a J_a \sum_{\langle i,j \rangle_a} S_i S_j, \quad (1)$$

where $a = 1, 2, 3$ means nearest-neighbor, next-nearest-neighbor, third-nearest-neighbor interactions, as shown in Fig. 1. From a programming perspective, compressing a hexagonal lattice into a brick wall lattice is more straightforward to implement, as the coordinates and indices of the lattice sites are integers. Thus, we compress it into a brick wall lattice to discuss various phases.

B. Wang-landau algorithm

In actual simulations, the cluster algorithm fails to capture the true correlations between spins and thus becomes ineffective [23]. We also do not resort to the Metropolis algorithm because, at low temperatures, the system has a high degree of degeneracy, making it difficult to achieve ergodicity [24].

Before the development of the WL method, several extended ensemble methods were proposed to improve sampling efficiency in systems with rough energy landscapes. These include the multicanonical ensemble [25, 26], entropic sampling [27], and the broad histogram Monte Carlo method [28]. The WL algorithm performs a random walk in the energy space by randomly flipping spin states [15–19]. The energy E associated with the spin configuration is accepted with a probability proportional to the reciprocal of its density of states $g(E)$, and $g(E)$

is updated and recorded during the simulation. In the random walk, to traverse the entire energy space, a cumulative histogram $H(E)$ is introduced: each time the energy E is visited, the corresponding value of $H(E)$ increases by 1. Eventually, the visit distribution $H(E)$ for each energy E is obtained. A flat energy histogram indicates that each energy is visited uniformly. The WL algorithm has been continuously evolving. People have been improving its accuracy, convergence speed, and so on from multiple perspectives [29–38], and this algorithm has also been widely applied to frustrated spin or tricritical spin systems [39–45] and other respects [46, 47]. This method was also applied to the $J_1 - J_2$ Ising model in generalized triangular lattices [48].

The specific steps of the WL algorithm are as follows:

- (1) Set the initial spin state of the entire lattice, initialize the density of states $g(E) = 1$ for all possible energies E , and set a modification factor, for example $f = 2$.
- (2) Randomly flip a spin to form a trial state. If the energy changes from E_{old} (before flipping) to E_{new} (after flipping), the transition probability from E_{old} to E_{new} is given by:

$$P(E_{\text{old}} \rightarrow E_{\text{new}}) = \min \left(\frac{g(E_{\text{old}})}{g(E_{\text{new}})}, 1 \right) \quad (1)$$

If $g(E_{\text{new}}) \leq g(E_{\text{old}})$, the flipped state is accepted. Otherwise, it is randomly accepted with a probability of $\frac{g(E_{\text{old}})}{g(E_{\text{new}})}$. - If the flipped state is accepted, update the density of states to $g(E_{\text{new}}) \rightarrow g(E_{\text{new}}) \times f$, and update the energy histogram: $H(E_{\text{new}}) \rightarrow H(E_{\text{new}}) + 1$. - If the random walk state is rejected and remains at the same energy E_{old} , multiply the existing density of states by f , that is, $g(E_{\text{old}}) \rightarrow g(E_{\text{old}}) \times f$, and update the energy histogram: $H(E_{\text{old}}) \rightarrow H(E_{\text{old}}) + 1$. Since $g(E)$ can become very large, the algorithm uses the logarithm of the density of states in practice, i.e. $\ln[g(E)] \rightarrow \ln[g(E)] + \ln(f)$.

- (3) Continue to execute step (2) until the histograms flatten, then reduce the modification factor using $f_1 = \sqrt{f}$.
- (4) Repeat steps (2) and (3) until $f = f_{\min}$, and the final density of states $g(E)$ is obtained.

In practical simulations, there are many hyperparameters to choose from, such as the value of f_{\min} , the criteria for judging flatness, how many evolution steps to perform before each flatness check, and whether all energy levels are subject to flatness checks, etc.

C. The parallel tempering method

PT is a simulation approach that boosts the efficiency of Monte Carlo (MC) sampling techniques [49], prov-

ing particularly valuable in frustrated and spin-glass systems [50, 51]. We employ this method as it produces more dependable simulation outcomes when $J_3 = 0.2$. The fundamental concept underlying the PT approach involves simulating multiple system replicas at distinct temperatures concurrently. Each replica serves as a copy of the system, featuring an identical set of spins but operating at a different temperature. The acceptance probability for an exchange between adjacent replicas adheres to:

$$p = \min \left(1, e^{(E_i - E_{i+1}) \left(\frac{1}{T_i} - \frac{1}{T_{i+1}} \right)} \right), \quad (2)$$

where $T_{i(i+1)}$ denotes the temperature of the respective replica, and $E_{i(i+1)}$ stands for the energy of the replica at temperature $T_{i(i+1)}$. The method has also been used to simulate the Ising-XY model successfully [52].

D. The measured quantities

The measured quantities include the following:

- The energy $U(T)$, which can be obtained using the relation:

$$U(T) = \frac{\sum_E E g(E) e^{-E/T}}{\sum_E g(E) e^{-E/T}} \quad (3)$$

- The specific heat $C_V(T)$, derived from the internal energy through the thermodynamic relation:

$$C_V = \frac{dU(T)}{dT} = \frac{\langle E^2 \rangle - \langle E \rangle^2}{NT^2} \quad (4)$$

III. RESULTS

We first discuss the zero temperature phase diagram, as well as the configurations of each phase and the corresponding structure factors. Then, we proceed to discuss the finite-temperature phase diagram for $J_3/J_1 = 1.2, 0.6$, and 0.2 , the exponents y_t of continuous phase transitions, and evidence for first-order phase transitions and specific heat multipeak phenomenon.

The zero-temperature phase diagram has been shown in Refs. [13, 14] in the range $-2 \leq J_2/J_1 \leq 0$ and $0 \leq J_3/J_1 \leq 2$ and a work about a real material experiment [11]. To compare with previous works [11, 13, 14], this paper also provides the zero-temperature phase diagram for this parameter range.

A. The results at $T = 0$

1. The global phase diagram at $T = 0$

Figure 2 presents the phase diagram of the ground state, which includes the stripe phase, the AC+SP phase,

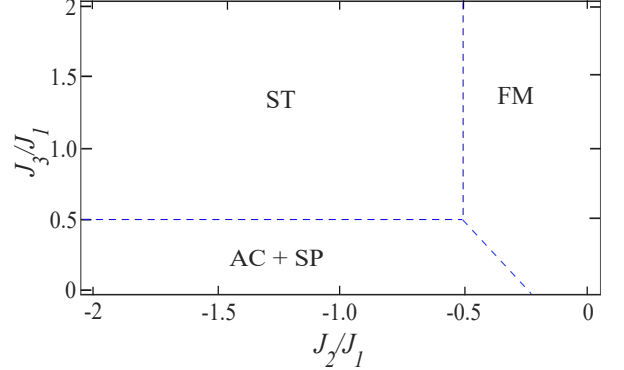


Figure 2. Phase diagram at zero temperature, which contains the ST, FM, and AC+SP phases. Different from Ref. [13], we find the AC phase should be coexist with the SP phase.

and the FM phase. The boundaries of the three phases can be solved analytically through energy calculations. The energy expressions per site for the three phases are as follows:

$$E_{\text{AC+SP}} = -\frac{J_1 - 2J_2 - J_3}{2}, \quad (5)$$

$$E_{\text{ST}} = \frac{J_1 + 2J_2 - 3J_3}{2}, \quad (6)$$

$$E_{\text{FM}} = -\frac{3J_1 + 6J_2 + 3J_3}{2}. \quad (7)$$

Setting $E_{\text{AC+SP}} = E_{\text{ST}}$, we obtain the boundary between the AC and ST phases as $J_3/J_1 = 1/2$. By setting $E_{\text{AC+SP}} = E_{\text{FM}}$, the boundary between the AC+SP and FM phases is in terms of $J_3/J_1 = -2J_2/J_1 - 1/2$. Furthermore, the ST-FM boundary is given by $J_2/J_1 = -1/2$ using the same method.

2. The typical configurations

In Fig. 3, the ground state spin configurations obtained from the WL sampling are shown. Figures 3 (a1)-(a4) show representative configurations of the AC phase, while Figs. 3 (b1)-(b16) correspond to various configurations in SP phase. Orange and blue dots indicate spin-up and spin-down orientations, respectively. It can be clearly seen that the degeneracy of the AC phase is four. Specifically, configurations (a2)-(a4) can be obtained by sequentially shifting the stripes of (a1) to the right, which reflects the invariance under horizontal translation. Due to the asymmetry between the horizontal and vertical directions of the lattice structure, these four vertical stripes do not have horizontal counterparts, unlike those of the square lattice [53]. In Figs 3 (a1)-(a4), the Hamiltonian exhibits space discrete translational symmetry along the horizontal-direction, satisfying $\mathcal{T}_x^1 H \mathcal{T}_x^{-1} = H$, and also possesses \mathbb{Z}_2 symmetry under global spin flip.

In Figs. 3 (b1)-(b16), the spiral configurations are shown. The red lines and arrows indicate the spiral direction of spin configurations. In Fig. 3 (b1), the first four

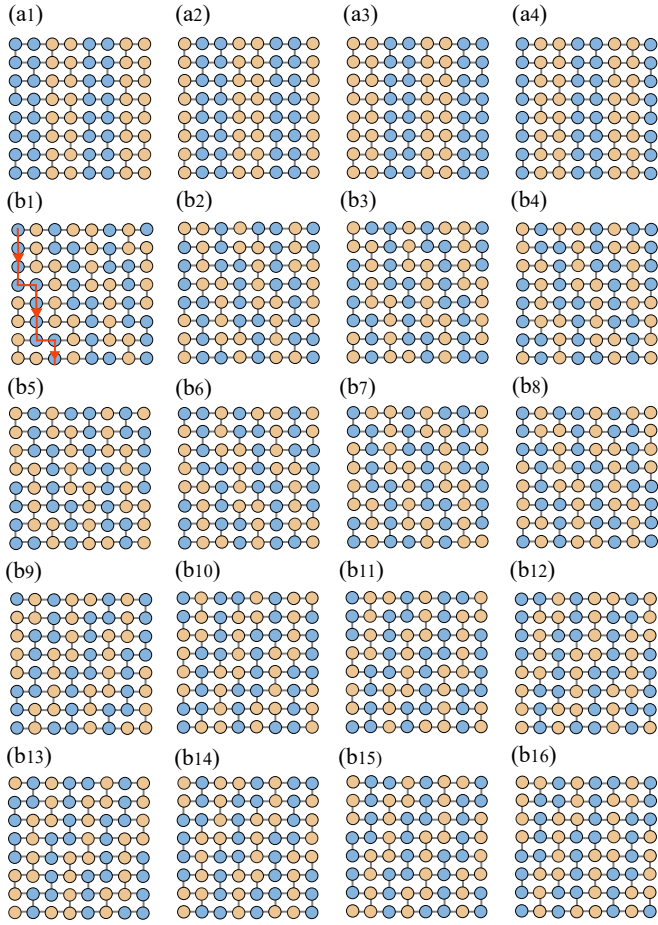


Figure 3. Ground state spin configurations obtained from WL sampling. (a1)-(a4) show configurations of the AC phase, while (b1)-(b16) correspond to various spiral configurations. These 20 configurations are degenerate, which has not been found in previous works [11, 13, 14]. Red lines and arrows in (b1) indicate the spiral direction of spin configurations.

elements in the first column are blue circles. Then, the fourth blue circle moves to the second column, followed by another four blue circles displayed downward. At the end of the blue column, it moves to the right again. Due to the periodic boundary condition, there are only 2 blue circles at the bottom of the third column, while the other two blue circles roll to the topmost position. In this way, the blue circles spread throughout the lattice and eventually return to the starting point. Figs. 3 (b2)-(b8) are similar by moving the first four blue circles down one by one. In Figs. 3 (b9)-(b16), the configurations can be obtained by applying the x -coordinate mapping $x \rightarrow 9 - x$ to the configurations shown in Figs. 3(b1)-(b8). In this Appendix A, a specific SP configuration on the hexagonal lattice is shown.

From a symmetry perspective, the configurations exhibit discrete translational symmetry along the vertical direction. For any single-step vertical translation operation \mathcal{T}_y , the energy of the configuration is invariant under

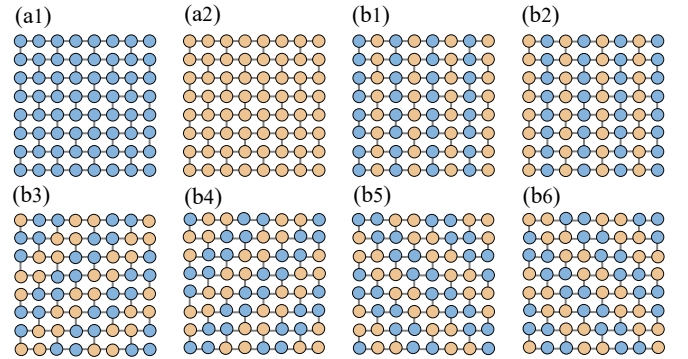


Figure 4. Ground-state spin configurations for (a1)-(a2) the FM phase and (b1)-(b6) the ST phase.

its action, satisfying

$$\mathcal{T}_y^n \mathcal{C} \mathcal{T}_y^{-n} = \mathcal{C}, \quad E(\mathcal{C}) = E(\mathcal{T}_y^n \mathcal{C}), \quad (8)$$

Here \mathcal{C} represents any configuration in the first subset, $n = 1, 2, \dots, 8$ is the number of translation steps, and $E(\mathcal{C})$ denotes the energy of configuration \mathcal{C} . The configurations also possess reflection symmetry with

$$\mathcal{R}_{x \rightarrow 9-x} \mathcal{C}_i \mathcal{R}_{x \rightarrow 9-x}^{-1} = \mathcal{C}'_i. \quad (9)$$

Here $\mathcal{R}_{x \rightarrow 9-x}$ is the mirror reflection operator, with \mathcal{C}_i ($i = 1, \dots, 8$) corresponding to b_1-b_8 and \mathcal{C}'_i ($i = 1, \dots, 8$) denoting Figs. 3 (b9)-(b16).

The spiral state has the properties defined in Refs. [2–5]. Generally, the spin structure factors of these spiral spin states exhibit discrete bright spots in momentum space at low temperatures, while forming rings at high temperatures or under strong quantum fluctuations. The contour of the ring in momentum space can be observed experimentally [54, 55]. The spiral state in this paper is defined differently. As defined in Refs. [5, 56], at the lower temperature, the peaks of the spin structure factor in momentum spaces are located at $(\pm k_1, \pm k_2)$, and in the real space, the configuration has spiral properties.

In Fig. 4, we also present the configuration of the FM phase and the ST phases. Among the ST phase, the stripes in Figs. 4 (b1) and (b2) are along the vertical direction, with the spin directions of the odd columns and even columns being opposite to each other. Figs. 4(b3) and (b4) also show the ST phase, where the stripe width is 2 and the stripes are tilted at a 45-degree angle, similar to the shape of “//”. In Figs. 4 (b5) and (b6), the tilt direction is like “\\”. In (b3)-(b6), these four configurations possess not only Z2 symmetry but also 90° rotational symmetry.

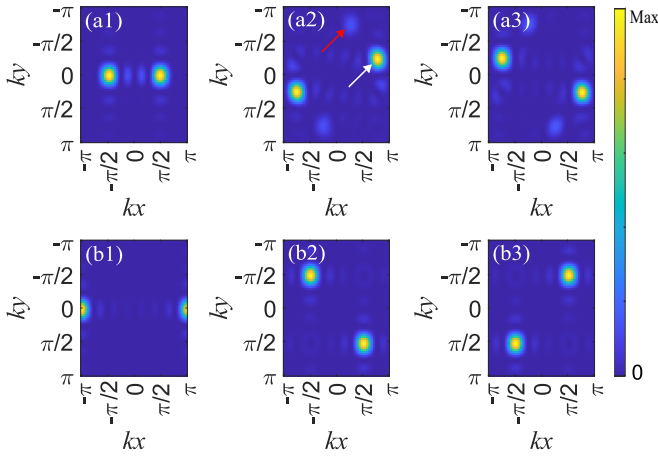


Figure 5. Structure factors corresponding to different configurations: (a1) for the AC phase; (a2) and (a3) is for the SP configurations; (b1)-(b3) for the ST configurations.

3. The spin structural factors

To further characterize the phases, we define the spin structure factor for the spins as

$$S(kx, ky) = \frac{1}{N} \sum_{i,j}^N e^{i\mathbf{k} \cdot (\mathbf{r}_i - \mathbf{r}_j)} \langle S_i S_j \rangle, \quad (10)$$

where N is number of spins. \mathbf{r}_i and \mathbf{r}_j are the coordinates of the spins, S_i and S_j are the values of spins. In the analysis of magnetic phases, the structure factor $S(\vec{k})$ provides critical insight into the spatial ordering of spin configurations. The presence of peaks in reciprocal space is directly related to the periodicity and symmetry of the real-space spin arrangements.

In Fig. 5, structure factors corresponding to different configurations are shown. In Fig. 5 (a1), the bright spots in $(\pm\pi/2, 0)$ correspond to the four AC configurations depicted in Figs. 3 (a1)-(a4). In the AC state, the translation-invariant period length $\Delta x_{AC} = 4$, and the relation $k = \pm 2\pi/\Delta x$ result in the wavevector positions $k_x = \pm\pi/2$. This solid phase with a period of 4 has also been observed in Rydberg atoms with long-range interactions [57, 58]. In Fig. 5 (a2), the bright spot pointed by the white arrow shows peaks at $k_y = \pm\pi/4$ and the bright spot pointed by the red arrow displays peaks at $k_x = \pm\pi/4$. These vectors $(\pm\pi/4, \pm\pi/4)$ correspond to the translation-invariant wave vector where $\Delta x = 8$ or $\Delta y = 8$ of the SP configurations, similar to the results in Refs. [5, 56]. In Fig. 5 (b1), bright spots in $(\pm\pi, 0)$ as a result of the two vertical stripes in the ST phase, where $\Delta x_{ST} = 2$. In Figs. 5 (b2)-(b3), $(\pm\pi/2, \pm\pi/2)$ means the four diagonal stripes as shown in Figs. 4 (b3)-(b6). The data in the figure are the results for $L = 8$, and other smaller dark spots are caused by the size effect, and these dark spots will disappear as the size increases.

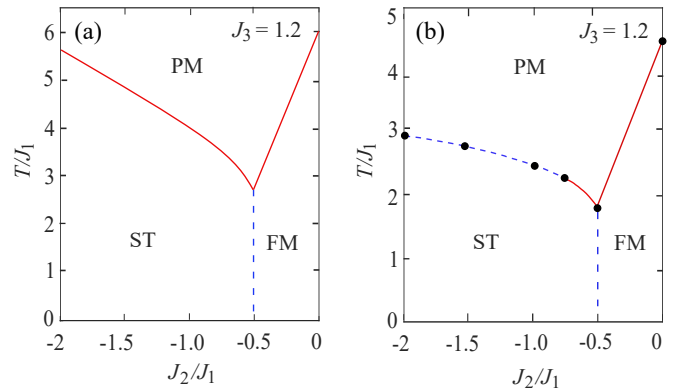


Figure 6. Finite-temperature phase diagram of $J_3/J_1 = 1.2$ (a) from Ref. [13] by the MF method (b) by the WL method. Solid lines indicate continuous phase transitions, whereas dashed lines represent first-order transitions. The tri-critical point is about $J_2/J_1 \approx -0.75$.

B. The phase diagram at $T > 0$

1. $J_3/J_1 = 1.2$

Based on the zero-temperature phase diagram in the J_3/J_1 - J_2/J_1 parameter space, we fix $J_3 = 1.2$ and plot the finite-temperature phase diagram in the J_2/J_1 - T/J_1 parameter space. For ease of comparison, we have included the phase boundaries of the MF method in Refs [13, 14], in Fig. 6(a), while the phase boundaries obtained from the WL algorithm are shown in Fig. 6(b). Solid lines represent continuous phase transitions, and dashed lines represent first-order phase transitions. In general, the topological structure of the phase diagrams is the same. The ST phase is located in the lower-left corner, the FM phase in the lower-right corner, and the paramagnetic phase in the high-temperature region.

There are differences in the nature of the phase transitions between the two methods. For example, in the region where $J_2/J_1 < J_2^c/J_1$ and $J_2^c/J_1 \approx -0.75$, the WL method reveals that the system undergoes a first-order phase transition, rather than the continuous phase transition identified by the MF algorithm. The strength of the WL algorithm lies in its ability to calculate the density of states more accurately, allowing the calculation of energy and its distribution $P(E, T)$ at different temperatures T . The double peaks at $T = T_c$ confirm the first-order transitions. For the range $J_2/J_1 > J_2^c/J_1$, the transitions are confirmed *continuous*. Sharp peaks in the specific heat help us to precisely obtain the critical exponent y_t .

Calculations of the critical exponents reveal that the phase transition type does not necessarily belong to the Ising universality class, since the ground state of the system has a degeneracy of six. For instance, at $J_2 = -0.75$, an energy bimodal distribution is observed, but the width of the bimodal peaks gradually decreases with increasing system size. The transition thus remains continuous.

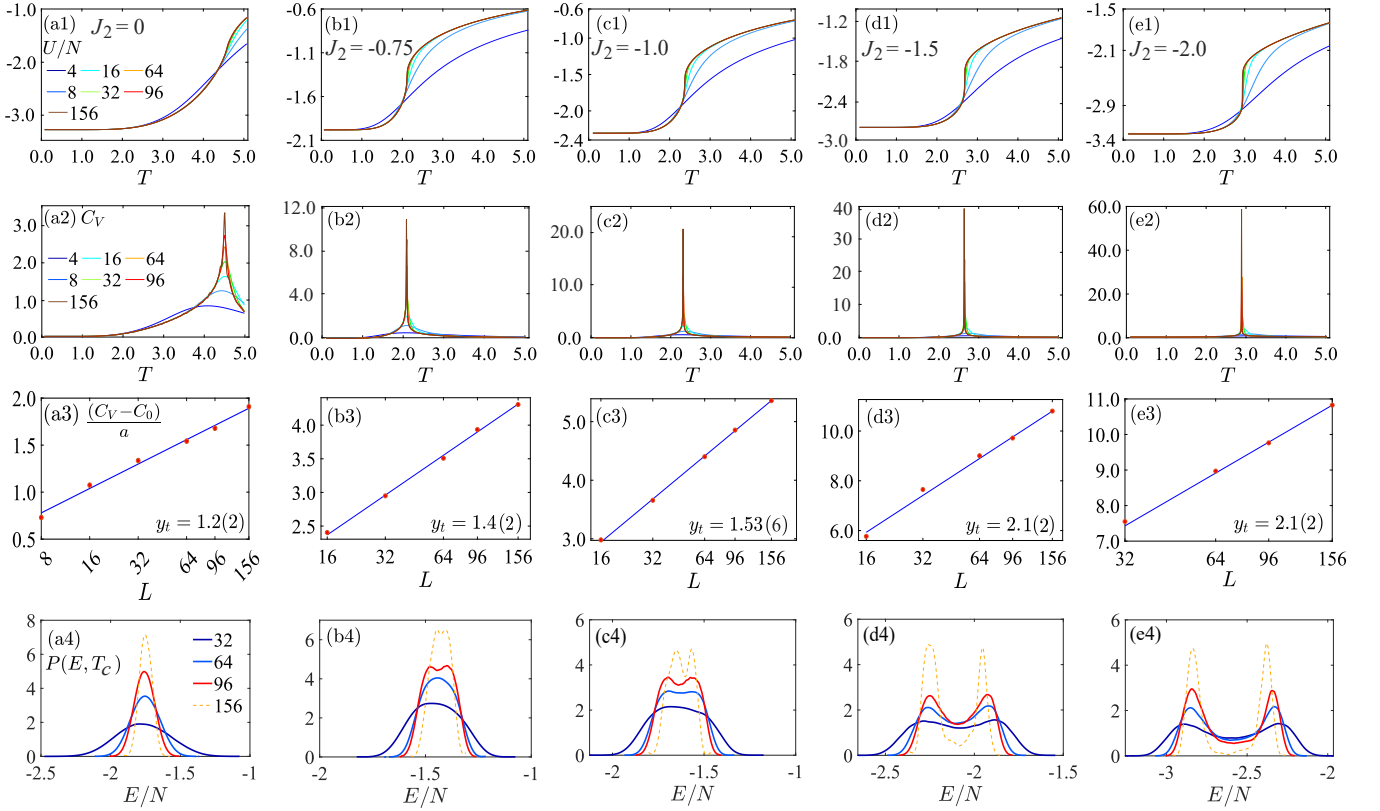


Figure 7. Details U/N , C_V , fitting of exponent y_t , and normalized distribution $P(E/N, T_c)$ are shown for $J_3 = 1.2$. For each columns, the parameters are $J_2/J_1 = 0, -0.75, -1, -1.5, -2$, respectively. The first two columns correspond to continuous phase transitions, while the last three columns correspond to first-order phase transitions.

This behavior is highly analogous to that of the four-state Potts model reported in Ref. [53], which is proven to exhibit a continuous phase transition.

In Fig. 7, details of fixing $J_3 = 1.2$ and scanning T/J_1 are shown. The first row shows the relationship between the average energy U/N and temperature when $J_2/J_1 = 0, -0.75, -1, -1.5$ and 2. At low temperatures ($T < T_c$) and high temperatures (e.g., $T = 5$), the energies of different sizes ($L \geq 8$) are convergent, as expected. Meanwhile, the values of these ground-state energy densities must be in accordance with Eq. 6. Each curve of energy versus temperature has undergone strict convergence testing, such as increasing the number of iteration steps, imposing stricter flatness conditions for histogram $H(E)$, and using values of f_{min} closer to 1.

In Fig. 7, the second row presents the relationship between specific heat C_V and temperature T . We divide the temperature range from 0 to 5 with an interval of 5×10^{-5} . Then, according to Eq. 4, we calculate the specific heat for different sizes. Each specific heat curve has a peak. The critical temperature $T_c(L)$, determined from the peaks of the specific heat, is retained in the fourth decimal place; Then, using the software “gnuplot”, the phase transition point in the thermodynamic limit is obtained via linear fitting with the least squares method and recorded in Tab. I and serve as a reference for other

Table I. Fitting results for the C_V using the ansatz Eq. 11 at $J_3/J_1 = 1.2$. The numbers in parentheses indicate errors, representing three times the standard deviation.

J_2/J_1	y_t	T_c	Type
0	1.2(2)	4.513(9)	continuous
-0.75	1.4(2)	2.085(3)	continuous
-1.0	1.53(6)	2.316(2)	first order
-1.5	2.1(2)	2.643(2)	first order
-2.0	2.1(2)	2.876(2)	first order

methods, such as the tensor network methods [59–64].

The critical exponent y_t can be fitted using the following finite-size scaling formula [65]:

$$C_V^{\max}(L) = C_0 + L^{2y_t-d}(a + bL^{y_1}), \quad (11)$$

where $C_V^{\max}(L)$ is the specific-heat to be fitted, L is the size of the lattice, C_0 , a , and b are constants, and d is the spatial dimension. In the fitting process, $b = 0$ is used, and the specific heat values used are the maximum values of the specific heat C_V^{\max} for different lattice sizes. In Fig. 7, data points $(C_V^{\max}(L) - C_0)/a$ versus L are plotted on a log-log scale, with those of different sizes all lying on the straight line fitted. The fitted results of y_t

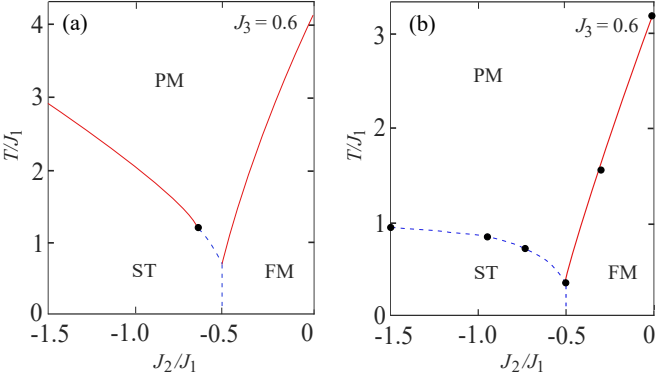


Figure 8. Finite temperature phase diagram of $J_3 = 0.6$ (a) from Ref. [13] by the MF method (b) by the WL method. Solid lines indicate continuous phase transitions, whereas dashed lines represent first-order transitions.

are shown on Tab. I.

For $J_2/J_1 = 0$, increasing the temperature T , the systems undergo a transition between the FM and PM phases, which is the standard Ising type. Using Eq. 11, the exponent $y_t = 1.1(2)$ is obtained as expected. For the Ising transition, the exponent $\alpha = 2y_t - d = 0$, means the logarithmic divergence of C_V^{\max} [66], which obeys the equations as follows.

$$C_V^{\max}(L) = C_0 + C_1 \ln L. \quad (12)$$

The values of $C_V^{\max}(L)$ at the Ising types of transition are also fitted using the above equation. For $J_2/J_1 = -0.75$ and $J_2/J_1 = -1.0$, the exponents $y_t = 1.4(2)$ and $y_t = 1.53(6)$ are obtained. These exponents are below 2, indicating the absence of a clear first-order phase transition at least for system sizes $L \leq 156$. For $J_2/J_1 = -1.5$ and -2.0 , the critical exponents are both $y_t = 2.1(2)$. The latter values are close to 2 within the error bar when considering the standard deviation three times. Substituting y_t into Eq. 4 yields the specific heat's divergence with system size, scaled as L^d , which signals a clear first-order phase transition [67].

The density of states $g(E)$ using the WL algorithm, multiplied by $e^{-E/T}$ gives the Boltzmann weight. For a first-order phase transition, a bimodal distribution can be obtained by finely tuning the temperature T and selecting an appropriate critical temperature $T = T_c$. As shown in Figs. 7 (b4) and (c4), for the largest system size achievable $L = 156$, a weak bimodal energy distribution is observed. This indicates that the system undergoes a weak first-order phase transition within the observed size range. The obvious double peaks emerge in Figs. 7 (d4) and (e4), corresponding to $J_2 = -1.5$ and $J_2 = -2$.

2. $J_3/J_1 = 0.6$

We now fix $J_3/J_1 = 0.6$ and plot the finite-temperature phase diagram. This parameter is closer to the boundary

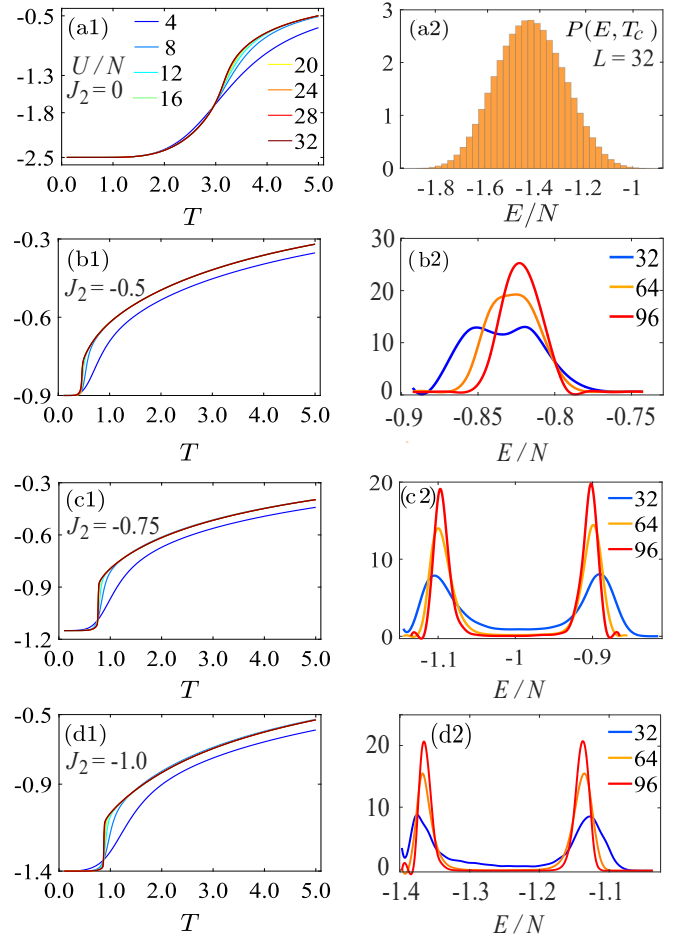


Figure 9. The first column shows U/N versus T at $J_3/J_1 = 0.6$. The second column displays the energy distribution at the phase transition point. The double peak indicates that the system undergoes a first-order phase transition. For each row, the parameter is $J_2/J_1 = 0, -0.5, -0.75$ and -1.0 , respectively.

$J_3/J_1 = 0.5$ at $T = 0$ in Fig. 2, and therefore the transitions are possible different from $J_3/J_1 = 1.2$ in the previous sections. Actually, for the ST-PM phase transition, the WL results differ significantly from the mean-field results: MF finds a tricritical point, whereas WL reveals that it is first-order phase transition.

In Fig. 8 (a), the phase boundaries are obtained using the MF method, while Fig. 8 (b) presents the results of the WL algorithm. The ST phase, the FM phase, and the PM phase: in the two phase diagrams, the positions of these three phases are consistent. The nature of phase boundaries obtained from the MF and WL methods differs. According to the MF method, the region $-0.78 < J_2/J_1 < -0.5$ exhibits first-order transitions, with continuous transitions elsewhere. In contrast, the WL algorithm identifies a broader first-order region, ranging from $-1.5 < J_2/J_1 < -0.5$, which is inconsistent with the tricritical and continuous transition scenarios predicted by the MF method.

Details of the first-order transition identified by the

WL algorithm are presented in Fig. 9. The first column displays U/N versus T , while the second column shows the energy distribution at the transition point. In Fig. 9 (a1), the energy shows a smooth upward slope and the single peak of $P(E/N, T_c)$ in Fig. 9 (a2) indicates the continuous phase transitions for $J_2/J_1 = 0$. In Figs. 9 (b1) and (b2), although obvious energy jumps are observed, and double peaks are detected for small system sizes (e.g., $L = 32$) the double peaks have clearly vanished for $L = 64$ and $L = 96$. This indicates that the phase transition here remains an continuous phase transition. In Figs. 9 (c1), (c2), (d1), and (d2) at $J_2/J_1 = -0.75, -1, -1.5$, the energies exhibit a jump as the temperature increases. This indicates a latent heat of phase transition, a hallmark of first-order phase transitions. The presence of a double-peak structure in the distribution confirms the conclusion.

The results of exponents y_t are $1.00(3), 1.2(2), 1.9(1), 1.9(1), 2.2(3)$, corresponding to the parameter sets with $J_2/J_1 = 0, -0.5, -0.75, -1, -1.5$ (where $J_3/J_1 = 0.6$ is fixed for all cases) respectively. Specifically, for the first two parameters, i.e., when $J_2/J_1 = 0$ and -0.5 , the obtained y_t values are consistent with the behavior of an Ising phase transition. For the latter three parameter sets ($J_2/J_1 = -0.75, -1, -1.5$), the y_t exponents align with the characteristics of a distinct first-order phase transition. Three sets of behaviors are in agreement with that exhibited by the bimodal energy distribution. The results are summarized in Table II.

Table II. Fitting results for the C_V using the ansatz Eq. 11 at $J_3/J_1 = 0.6$. The numbers in parentheses indicate errors, representing three times the standard deviation.

J_2/J_1	y_t	T_c	Type
0	$1.00(3)$	$3.134(1)$	Ising type
-0.5	$1.2(2)$	$0.454(3)$	Ising type
-0.75	$1.9(1)$	$0.758(1)$	first order
-1.0	$1.9(1)$	$0.859(6)$	first order
-1.5	$2.2(3)$	$0.963(3)$	first order

3. $J_3/J_1 = 0.2$

In this section, we fix $J_3 = 0.2$ and plot the finite-temperature phase diagram in the J_2/J_1 - T/J_1 plane. In Fig. 10(a), we show the phase boundaries obtained using the MF method, while Fig. 10(b) presents the results from the PT and WL algorithms. The AC+SP phase is observed in the lower-left corner of the phase diagram, which differs from previous results where only the AC phase was identified [11, 13].

Within the range $-1 < J_2/J_1 < -0.35$, elevating the temperature induces distinct first-order phase transitions between the SP+AC phase and the paramagnetic (PM) phase. In contrast, within $-1.5 < J_2/J_1 < -1$, temperature elevation similarly triggers evident first-order phase

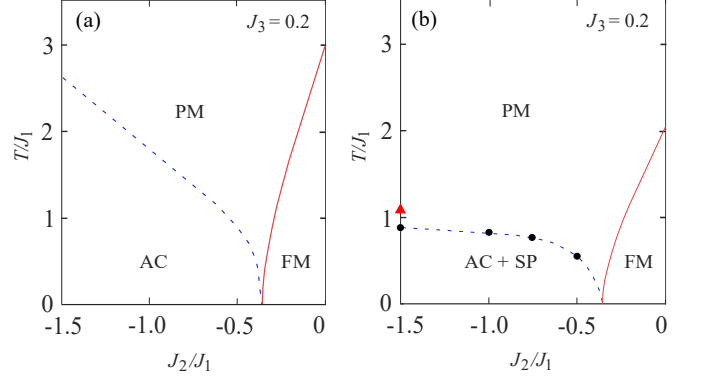


Figure 10. Finite temperature phase diagram of $J_3/J_1 = 0.2$ (a) from Ref. [13] by the MF method (b) by the WL method. Solid lines indicate continuous phase transitions, whereas dashed lines represent first-order transitions. Multi-peak phenomenon in specific heat observed near red-triangle-marked positions at $J_2/J_1 = -1.5$.

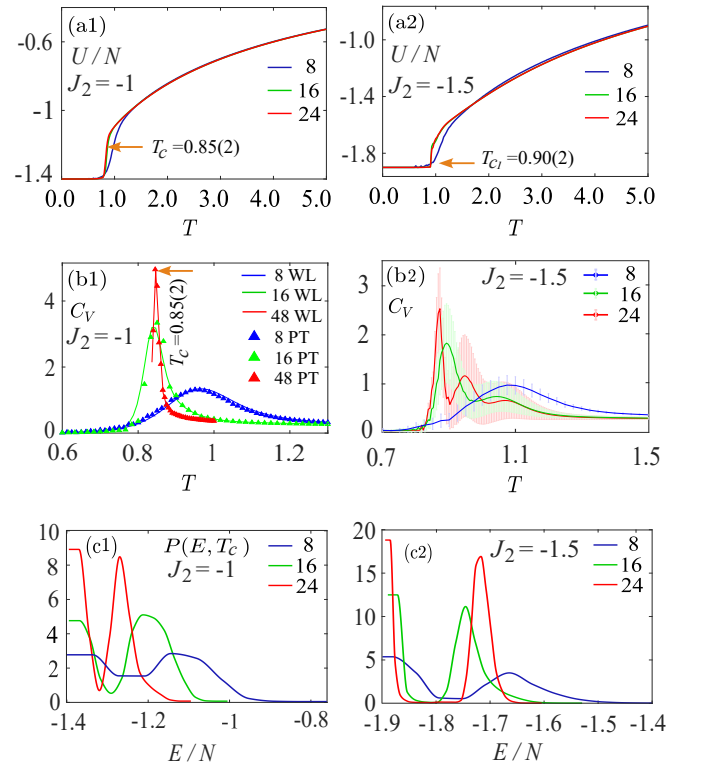


Figure 11. At $J_3/J_1 = 0.2$, the temperature dependences of (a) the energy, (b) the specific heat, as well as (c) the double-peak distribution of the energy for various system sizes. Left column: $J_2/J_1 = -1$; Right column: $J_2/J_1 = -1.5$.

transitions; additionally, extra peaks emerge in the specific heat curve—an experimental signature of competing interactions in frustrated systems that underpins the first-order phase transition behavior. Notably, the number of these peaks is dependent on the lattice size: for example, lattices with $L = 8, 16$, and 24 exhibit 1, 2, and 3 specific heat peaks, respectively.

Figure 11 illustrates the detailed characteristics of the phase transitions. Specifically, the left and right columns of the figure correspond to the cases with $J_2 = -1$ and $J_2 = -1.5$, respectively. Panels (a1) and (a2) of Fig. 11 plot the curves of U/N versus T , where energy jumps are observed at the critical temperatures $T_c = 0.85(2)$ and $T_c = 0.90(2)$, respectively. These energy jumps confirm the occurrence of first-order phase transitions, and the evidence for such transitions is conclusive: for example, the bimodal distributions of energy, which are clearly shown in Figs. 11(c1) and (c2) and they become increasingly pronounced with increasing lattice size.

For $J_2 = -1$, only a single specific heat peak is observed across different lattice sizes; notably, the peak for the large lattice ($L = 48$) is located at $T_c = 0.85(2)$. In contrast, stronger frustration interactions arise for $J_2 = -1.5$, making the WL method unable to yield reliable results. Thus, we adopt the PT method to simulate the system, with thermal parameters set as follows: 5×10^6 thermal steps, 2×10^4 bins, 1000 Monte Carlo steps, and 200 temperature points distributed in the range of 0.5 to 1.5. Although the error bars of the specific heat remain relatively large, the multi-peak phenomenon is still distinctly observable.

Notably, in PT simulations, the AC configuration is directly adopted as the initial configuration in the low-temperature region. Compared with random initial configurations, results from the AC configuration exhibit smoother behavior after a sufficient number of thermalization steps.

For Fig. 11(c1), we adopt the temperatures of 0.984, 0.853, and 0.8285 for lattice sizes $L = 8, 16$, and 24, respectively, for the construction of the equal-height profile. It should be emphasized that these chosen temperatures are not required to exactly match the thermodynamic transition temperature T_c . For Fig. 11(c2), the temperatures corresponding to the same lattice sizes and equal-height criterion are 1.0234, 0.941, and 0.930, respectively.

4. The multipeak phenomenon of specific heat

As described in Ref. [22], the commonly observed multiple-peak behavior of specific heat corresponds to the Schottky anomaly [68–70], where the specific heat exhibits an anomalous sharp peak in addition to the conventional one. This phenomenon exists in non-frustrated systems, such as the classical spin-1 system, e.g., the Blume-Capel model [44]. For frustrated real materials, the multi-peak Schottky effect has been experimentally observed [71–75]. From the perspective of phenomenological theory, Ref. [22] states that a system with n peaks should possess n parameters. For the system with size 24 investigated in this paper, three peaks are indeed observed, which correspond to the three parameters J_1, J_2 , and J_3 .

However, the multiple peaks in the specific heat here

are very likely a finite-size effect. Such effect has been studied in the $J_1 - J_2 - J_3$ Ising model in the square lattices by the MC method [76]. Subsequently, both the axial next-nearest-neighbor Ising (ANNNI) model and the biaxial next-nearest-neighbor Ising (BNNNI) model exhibit multiple peaks in their specific heat. In particular, for the ANNNI model with $J_2 = 0$ and finite J_3 along the horizontal axis, and the BNNNI model with $J_2 = 0$ and finite J_3 along both axes, a multi-peak structure in the specific heat is observed (see Fig. 1 in [77] and Fig. 10 in [78]). This feature is shown to be a finite-size signature characteristic of the incommensurate phase, evidenced by: (i) the number of peaks increases monotonically with increasing system size; and (ii) finite-size scaling analysis reveals that the extrapolated peak temperatures converge to a single point [79]. Due to the substantial computational demands in these strongly frustrated parameter regimes, our calculations are currently limited to $L = 24$. The investigation of specific heat peaks for larger system sizes is therefore left to future work.

IV. CONCLUSION AND DISCUSSION

In this work, we systematically reexamine the classical $J_1-J_2-J_3$ model on the honeycomb lattice via the WL algorithm, delivering new insights into the system's properties. We first clarify the degeneracy of the AC phase: contrary to prior reports of 4- or 12-fold degeneracy [13, 14], the AC phase exhibits 20-fold degeneracy, with 16 newly identified degenerate states corresponding to spiral configurations, which can be characterized by 4 bright spots in the momentum-space structure factor.

Regarding phase transitions, our WL results reveal distinct behaviors across parameter regimes: for $J_3/J_1 = 1.2$, the stripe (ST)-paramagnetic (PM) transition hosts a tricritical point near $J_2/J_1 \approx -0.75$, while the determination of more precise values requires extensive calculations and analyses [80–86], which fall beyond the scope of this paper. For $J_3/J_1 = 0.6$, the ST-PM transition is either first-order or first-order; when $J_3/J_1 = 0.2$, the AC+SP-PM transition also follows first-order behavior. In the strong frustration regime ($J_2/J_1 = -1.5$), we further observe multi-peak behavior in the specific heat [76, 77]. When $J_3 = 0$, our findings align with previous Metropolis and parallel tempering studies of the J_1-J_2 honeycomb model [66], confirming the consistency of our approach.

This work establishes a foundation for further exploration of the $J_1-J_2-J_3$ model. Future investigations will focus on higher-precision calculations of phase transition points and critical exponents, leveraging advanced methods such as tensor network Monte Carlo [61–64]. We also aim to extend the framework: incorporating external magnetic fields to map field-dependent phase diagrams, expanding parameter ranges to stronger frustration regimes, investigating high-spin generalizations [11], and extending the analysis to the quantum transverse-field

J_1 - J_2 - J_3 Ising model, for exploring quantum phase transitions that complement the classical thermal transitions studied here.

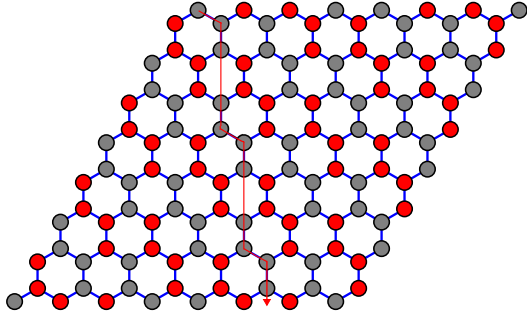


Figure 12. A typical configuration in the SP phase on the hexagonal lattice; arrows indicate the spiral direction.

Acknowledgements: We thank Yi Hu and Patrick Charbonneau for helpful discussions. W. Z. was supported by the Hefei National Research Center for Physical Sciences at the Microscale (Grant No. KF2021002) and the Fundamental Research Program of Shanxi Province (Grant Nos. 202303021221029). Y. J. was supported by the National Natural Science Foundation of China (Grant No. 12275263) and the Natural Science Foundation of Fujian Province of China (Grant No. 2023J02032).

Appendix A: A snapshot in the real honeycomb lattices

In the main text, to facilitate the observation of symmetries of the configuration such as translational symmetry and mirror reflection symmetry, we compress the hexagonal lattice into a brick-wall lattice for investigation. In this appendix, we directly place a specific SP configuration on the hexagonal lattice for easy reference.

[1] H. T. Diep, *Frustrated Spin Systems*, 3rd ed. (World Scientific Publishing Co. Pte. Ltd., 2020).

[2] J. Oitmaa and R. R. P. Singh, Phase diagram of the $J_1 - J_2 - J_3$ Heisenberg model on the honeycomb lattice: A series expansion study, *Phys. Rev. B* **84**, 094424 (2011).

[3] P. H. Y. Li, R. F. Bishop, D. J. J. Farnell, J. Richter, and C. E. Campbell, Ground-state phases of the frustrated spin-1/2 $J_1 - J_2 - J_3$ Heisenberg ferromagnet ($J_1 < 0$) on the honeycomb lattice with $J_3 = J_2 > 0$, *Phys. Rev. B* **85**, 085115 (2012).

[4] S. Jiang, S. R. White, and A. L. Chernyshev, Quantum phases in the honeycomb-lattice J_1 - J_3 ferro-antiferromagnetic model, *Phys. Rev. B* **108**, L180406 (2023).

[5] W.-Y. Liu, D. Poilblanc, S.-S. Gong, W.-Q. Chen, and Z.-C. Gu, Tensor network study of the spin- $\frac{1}{2}$ square-lattice J_1 - J_2 - J_3 model: Incommensurate spiral order, mixed valence-bond solids, and multicritical points, *Phys. Rev. B* **109**, 235116 (2024).

[6] F. Ferrari, S. Bieri, and F. Becca, Competition between spin liquids and valence-bond order in the frustrated spin- $\frac{1}{2}$ Heisenberg model on the honeycomb lattice, *Phys. Rev. B* **96**, 104401 (2017).

[7] S.-S. Gong, D. N. Sheng, O. I. Motrunich, and M. P. A. Fisher, Phase diagram of the spin- $\frac{1}{2}$ J_1 - J_2 Heisenberg model on a honeycomb lattice, *Phys. Rev. B* **88**, 165138 (2013).

[8] S.-S. Gong, W. Zhu, and D. N. Sheng, Quantum phase diagram of the spin-1 $J_1 - J_2$ Heisenberg model on the honeycomb lattice, *Phys. Rev. B* **92**, 195110 (2015).

[9] S. R. White, Density matrix formulation for quantum renormalization groups, *Phys. Rev. Lett.* **69**, 2863 (1992).

[10] W.-Y. Liu, H. Zhai, R. Peng, Z.-C. Gu, and G. K.-L. Chan, Accurate simulation of the Hubbard model with finite fermionic projected entangled pair states, *Phys. Rev. Lett.* **134**, 256502 (2025).

[11] A. R. Wildes, D. Lançon, M. K. Chan, F. Weickert, N. Harrison, V. Simonet, M. E. Zhitomirsky, M. V. Gvozdikova, T. Ziman, and H. M. Rønnow, High field magnetization of FePS_3 , *Phys. Rev. B* **101**, 024415 (2020).

[12] P. Chanlert, N. Kurita, H. Tanaka, M. Kimata, and H. Nojiri, Collective and local excitations in $\text{Ba}_2\text{CoTeO}_6$: A composite system of a spin-1/2 triangular-lattice Heisenberg antiferromagnet and a honeycomb-lattice $J_1 - J_2$ Ising antiferromagnet, *Phys. Rev. B* **96**, 064419 (2017).

[13] P. Dias, A. Krindges, C. Morais, F. Zimmer, M. Móhlyna, M. Žukovič, and M. Schmidt, Residual entropy, bicriticality, and tricriticality in the frustrated Ising model on the honeycomb lattice, *J. Magn. Magn. Mater.* **604**, 172282 (2024).

[14] P. F. Dias and M. Schmidt, Zigzag phase transition in the frustrated Ising honeycomb lattice, *Phys. Rev. B* **108**, 014436 (2023).

[15] F. Wang and D. P. Landau, Efficient, multiple-range random walk algorithm to calculate the density of states, *Phys. Rev. Lett.* **86**, 2050 (2001).

[16] F. Wang and D. P. Landau, Determining the density of states for classical statistical models: A random walk algorithm to produce a flat histogram, *Phys. Rev. E* **64**, 056101 (2001).

[17] T. Vogel, Y. W. Li, T. Wüst, and D. P. Landau, Generic, hierarchical framework for massively parallel Wang-Landau sampling, *Phys. Rev. Lett.* **110**, 210603 (2013).

[18] L. Y. Barash, M. A. Fadeeva, and L. N. Shchur, Control of accuracy in the Wang-Landau algorithm, *Phys. Rev. E* **96**, 043307 (2017).

[19] S. Bi and N.-H. Tong, Monte Carlo algorithm for free energy calculation, *Phys. Rev. E* **92**, 013310 (2015).

[20] Y. L. Xie, P. Chu, Y. L. Wang, J. P. Chen, Z. B. Yan, and J.-M. Liu, Wang-Landau sampling with logarithmic windows for continuous models, *Phys. Rev. E* **89**, 013311 (2014).

[21] J. Colbois, B. Vanhecke, L. Vanderstraeten, A. Smerald, F. Verstraete, and F. Mila, Partial lifting of degeneracy in the $J_1-J_2-J_3$ Ising antiferromagnet on the kagome lattice, *Phys. Rev. B* **106**, 174403 (2022).

[22] E. Jurčišinová and M. Jurčišin, Multipeak low-temperature behavior of specific heat capacity in frustrated magnetic systems: An exact theoretical analysis, *Phys. Rev. E* **97**, 052129 (2018).

[23] R. H. Swendsen and J.-S. Wang, Nonuniversal critical dynamics in Monte Carlo simulations, *Phys. Rev. Lett.* **58**, 86 (1987).

[24] N. Metropolis, A. W. Rosenbluth, M. N. Rosenbluth, A. H. Teller, and E. Teller, Equation of state calculations by fast computing machines, *J. Chem. Phys.* **21**, 1087 (1953).

[25] B. A. Berg and T. Neuhaus, Multicanonical ensemble: A new approach to simulate first-order phase transitions, *Phys. Rev. Lett.* **68**, 9 (1992).

[26] B. A. Berg and T. Celik, New approach to spin-glass simulations, *Phys. Rev. Lett.* **69**, 2292 (1992).

[27] J. Lee, New Monte Carlo algorithm: Entropic sampling, *Phys. Rev. Lett.* **71**, 211 (1993).

[28] P. M. C. de Oliveira, T. J. P. Penna, and H. J. Herrmann, Broad histogram Monte Carlo, *Eur. Phys. J. B* **1**, 205 (1998).

[29] C. Zhou and R. N. Bhatt, Understanding and improving the Wang-Landau algorithm, *Phys. Rev. E* **72**, 025701(R) (2005).

[30] G. Brown, K. Odbadrakh, D. M. Nicholson, and M. Eisenbach, Convergence for the Wang-Landau density of states, *Phys. Rev. E* **84**, 065702(R) (2011).

[31] A. A. Caparica and A. G. Cunha-Netto, Wang-Landau sampling: Improving accuracy, *Phys. Rev. E* **85**, 046702 (2012).

[32] A. N. Morozov and S. H. Lin, Accuracy and convergence of the Wang-Landau sampling algorithm, *Phys. Rev. E* **76**, 026701 (2007).

[33] P. Poulain, F. Calvo, R. Antoine, M. Broyer, and P. Dugourd, Performances of Wang-Landau algorithms for continuous systems, *Phys. Rev. E* **73**, 056704 (2006).

[34] C. Zhou, T. C. Schulthess, S. Torbrügge, and D. P. Landau, Wang-Landau algorithm for continuous models and joint density of states, *Phys. Rev. Lett.* **96**, 120201 (2006).

[35] B. A. Berg and W. Janke, Wang-Landau multibondic cluster simulations for second-order phase transitions, *Phys. Rev. Lett.* **98**, 040602 (2007).

[36] D. P. Landau, S.-H. Tsai, and M. Exler, A new approach to Monte Carlo simulations in statistical physics: Wang-Landau sampling, *Am. J. Phys.* **72**, 1294 (2004).

[37] F. Wang and D. P. Landau, Determining the density of states for classical statistical models: A random walk algorithm to produce a flat histogram, *Phys. Rev. E* **64**, 056101 (2001).

[38] D. Perera, Y. W. Li, M. Eisenbach, T. Vogel, and D. P. Landau, Replica-exchange Wang—Landau sampling: Pushing the limits of Monte Carlo simulations in materials sciences, in *TMS 2015 144th Annual Meeting & Exhibition* (Springer International Publishing, Cham, 2016) pp. 811–818.

[39] C. J. Silva, A. A. Caparica, and J. A. Plascak, Wang-Landau Monte Carlo simulation of the Blume-Capel model, *Phys. Rev. E* **73**, 036702 (2006).

[40] K. Takeuchi, R. Tanaka, and K. Yuge, New Wang-Landau approach to obtain phase diagrams for multi-component alloys, *Phys. Rev. B* **96**, 144202 (2017).

[41] M. H. Qin, K. F. Wang, and J. M. Liu, Two-step magnetization in a spin-chain system on the triangular lattice: Wang-Landau simulation, *Phys. Rev. B* **79**, 172405 (2009).

[42] Y. Shevchenko, K. Nefedev, and Y. Okabe, Entropy of diluted antiferromagnetic Ising models on frustrated lattices using the Wang-Landau method, *Phys. Rev. E* **95**, 052132 (2017).

[43] M. Azhari and U. Yu, Tricritical point in the mixed-spin Blume-Capel model on three-dimensional lattices: Metropolis and Wang-Landau sampling approaches, *Phys. Rev. E* **102**, 042113 (2020).

[44] W. Kwak, J. Jeong, J. Lee, and D.-H. Kim, First-order phase transition and tricritical scaling behavior of the Blume-Capel model: A Wang-Landau sampling approach, *Phys. Rev. E* **92**, 022134 (2015).

[45] M. Azhari and U. Yu, Monte Carlo studies of the Blume-Capel model on nonregular two- and three-dimensional lattices: phase diagrams, tricriticality, and critical exponents, *J. Stat. Mech.* **2022**, 033204 (2022).

[46] F. Wang, W. Liu, J. Ma, K. Qi, Y. Tang, and Z. Di, Exploring transitions in finite-size Potts model: comparative analysis using Wang-Landau sampling and parallel tempering, *J. Stat. Mech.* **2024**, 093201 (2024).

[47] W. Liu, F. Wang, P. Sun, and J. Wang, Pseudo-phase transitions of Ising and Baxter-Wu models in two-dimensional finite-size lattices, *J. Stat. Mech.* **2022**, 093206 (2022).

[48] H. Jang and U. Yu, Monte Carlo study of frustrated Ising model with nearest- and next-nearest-neighbor interactions in generalized triangular lattices, *J. Stat. Mech.* **2024**, 073204 (2024).

[49] R. H. Swendsen and J.-S. Wang, Replica Monte Carlo simulation of spin-glasses, *Phys. Rev. Lett.* **57**, 2607 (1986).

[50] K. Binder and A. P. Young, Spin glasses: Experimental facts, theoretical concepts, and open questions, *Rev. Mod. Phys.* **58**, 801 (1986).

[51] M. Baity-Jesi, R. A. Baños, A. Cruz, L. A. Fernández, J. M. Gil-Narvion, A. Gordillo-Guerrero, D. Iñiguez, A. Maiorano, F. Mantovani, E. Marinari, V. Martin-Mayor, J. Monforte-Garcia, A. M. n. Sudupe, D. Navarro, G. Parisi, S. Perez-Gaviro, M. Pivanti, F. Ricci-Tersenghi, J. J. Ruiz-Lorenzo, S. F. Schifano, B. Seoane, A. Tarancón, R. Tripiccione, and D. Yllanes (Janus Collaboration), Critical parameters of the three-dimensional Ising spin glass, *Phys. Rev. B* **88**, 224416 (2013).

[52] H. Ma, W. Zhang, Y. Tian, C. Ding, and Y. Deng, Emergent topological ordered phase for the Ising-XY model revealed by cluster-updating Monte Carlo method, *Chinese Physics B* **33**, 040503 (2024).

[53] S. Jin, A. Sen, W. Guo, and A. W. Sandvik, Phase transitions in the frustrated Ising model on the square lattice, *Phys. Rev. B* **87**, 144406 (2013).

[54] N. D. Andriushin, S. E. Nikitin, Ø. S. Fjellvåg, J. S. White, A. Podlesnyak, D. S. Inosov, M. C. Rahn, M. Schmidt, M. Baenitz, and A. S. Sukhanov, Observation of the spiral spin liquid in a triangular-lattice ma-

terial, *N. Commun.* **16**, 2619 (2025).

[55] S. Gao, M. A. McGuire, Y. Liu, D. L. Abernathy, C. d. Cruz, M. Frontzek, M. B. Stone, and A. D. Christianson, Spiral spin liquid on a honeycomb lattice, *Phys. Rev. Lett.* **128**, 227201 (2022).

[56] L. Capriotti and S. Sachdev, Low-temperature broken-symmetry phases of spiral antiferromagnets, *Phys. Rev. Lett.* **93**, 257206 (2004).

[57] N. Chepiga and F. Mila, Kibble-Zurek exponent and chiral transition of the period-4 phase of Rydberg chains, *Nat. Commun.* **12**, 414 (2021).

[58] N. Chepiga, Tunable quantum criticality in multicomponent Rydberg arrays, *Phys. Rev. Lett.* **132**, 076505 (2024).

[59] H. Li and L.-P. Yang, Tensor network simulation for the frustrated J_1-J_2 Ising model on the square lattice, *Phys. Rev. E* **104**, 024118 (2021).

[60] K. Yoshiyama and K. Hukushima, Higher-order tensor renormalization group study of the J_1-J_2 Ising model on a square lattice, *Phys. Rev. E* **108**, 054124 (2023).

[61] M. Frías-Pérez, M. Mariën, D. P. García, M. C. Bañuls, and S. Iblisdir, Collective Monte Carlo updates through tensor network renormalization, *SciPost Phys.* **14**, 123 (2023).

[62] T. Chen, J. Liu, Y. Deng, and P. Zhang, Tensor network Markov chain Monte Carlo: Efficient sampling of three-dimensional spin glasses and beyond (2025), [arXiv:2509.23945 \[cond-mat.stat-mech\]](https://arxiv.org/abs/2509.23945).

[63] T. Chen, J. Zhang, J. Liu, Y. Deng, and P. Zhang, Batchtnmc: Efficient sampling of two-dimensional spin glasses using tensor network Monte Carlo (2025), [arXiv:2509.19006 \[cond-mat.stat-mech\]](https://arxiv.org/abs/2509.19006).

[64] T. Chen, E. Guo, W. Zhang, P. Zhang, and Y. Deng, Tensor network Monte Carlo simulations for the two-dimensional random-bond Ising model, *Phys. Rev. B* **111**, 094201 (2025).

[65] M. N. Barber, R. B. Pearson, D. Toussaint, and J. L. Richardson, Finite-size scaling in the three-dimensional Ising model, *Phys. Rev. B* **32**, 1720 (1985).

[66] M. Žukovič, Critical properties of the frustrated Ising model on a honeycomb lattice: A Monte Carlo study, *Physics Letters A* **404**, 127405 (2021).

[67] A. W. Sandvik, A. Avella, and F. Mancini, Computational studies of quantum spin systems, in *AIP Conference Proceedings* (AIP, 2010).

[68] N. P. Raju, E. Gmelin, and R. K. Kremer, Magnetic-susceptibility and specific-heat studies of spin-glass-like ordering in the pyrochlore compounds $R_2Mo_2O_7$ ($R = Y, Sm, or Gd$), *Phys. Rev. B* **46**, 5405 (1992).

[69] K. Ishida, M. Morishita, K. Yawata, and H. Fukuyama, Low temperature heat-capacity anomalies in two-dimensional solid 3He , *Phys. Rev. Lett.* **79**, 3451 (1997).

[70] A. P. Ramirez, Strongly geometrically frustrated magnets, *Annu. Rev. Mater. Res.* **24**, 453 (1994).

[71] D. Villuendas, T. Tsutaoka, and J. Hernández Ferràs, Heat capacity study of the magnetic phases in a Nd_5Ge_3 single crystal, *J. Magn. Magn Mater.* **405**, 282 (2016).

[72] M. Ito, T. Furuta, K. Kai, A. Taira, K. Onda, I. Shigeta, and M. Hiroi, Thermodynamic properties of Heusler $Fe_{2-x}Co_xMnSi$, *J. Magn. Magn Mater.* **428**, 390 (2017).

[73] Ł. Gondek, A. Szytuła, D. Kaczorowski, A. Szewczyk, M. Gutowska, and P. Piekarz, Multiple magnetic phase transitions in $Tb_3Cu_4Si_4$, *J. Phys.: Condens. Matter* **19**, 246225 (2007).

[74] P. Schobinger-Papamantellos, J. Rodríguez-Carvajal, L. D. Tung, C. Ritter, and K. H. J. Buschow, Competing multiple-q magnetic structures in $HoGe_3$: I. the magnetic phase diagram of $HoGe_3$, *J. Phys.: Condens. Matter* **20**, 195201 (2008).

[75] D. O'Flynn, M. R. Lees, and G. Balakrishnan, Magnetic susceptibility and heat capacity measurements of single crystal $TbMnO_3$, *J. Phys.: Condens. Matter* **26**, 256002 (2014).

[76] E. Rastelli, S. Regina, and A. Tassi, Specific heat and structure factor in the square ANNNI model by Monte Carlo simulation, *Phys. Rev. B* **81**, 094425 (2010).

[77] Y. Hu and P. Charbonneau, Resolving the two-dimensional axial next-nearest-neighbor Ising model using transfer matrices, *Phys. Rev. B* **103**, 094441 (2021).

[78] Y. Hu and P. Charbonneau, Numerical transfer matrix study of frustrated next-nearest-neighbor Ising models on square lattices, *Phys. Rev. B* **104**, 144429 (2021).

[79] Y. Hu and P. Charbonneau, Private communication (2025).

[80] B. Nienhuis, W. Guo, and H. W. J. Blöte, Tricritical $O(n)$ models in two dimensions, *Phys. Rev. E* **78**, 061104 (2008).

[81] Y. Deng, J. R. Heringa, and H. W. J. Blöte, Constrained tricritical phenomena in two dimensions, *Phys. Rev. E* **71**, 036115 (2005).

[82] Y. Deng and H. W. J. Blöte, Constrained tricritical Blume-Capel model in three dimensions, *Phys. Rev. E* **70**, 046111 (2004).

[83] Y. Deng and H. W. J. Blöte, Edge phase transitions of the tricritical Potts model in two dimensions, *Phys. Rev. E* **71**, 026109 (2005).

[84] Y. Deng, H. W. J. Blöte, and B. Nienhuis, Geometric properties of two-dimensional critical and tricritical Potts models, *Phys. Rev. E* **69**, 026123 (2004).

[85] Y. Deng and H. W. J. Blöte, Red-bond exponents of the critical and the tricritical Ising model in three dimensions, *Phys. Rev. E* **70**, 056132 (2004).

[86] H. W. J. Blöte and Y. Deng, Revisiting the field-driven edge transition of the tricritical two-dimensional Blume-Capel model, *Phys. Rev. E* **99**, 062133 (2019).